

# Modelling direction-dependent hardening in magnesium sheet forming simulations

Dirk Steglich · Wolfgang Brocks · Jan Bohlen ·  
Frederic Barlat

Received: 11 July 2010 / Accepted: 11 February 2011 / Published online: 9 March 2011  
© Springer-Verlag France 2011

**Abstract** In this work, a model capturing anisotropic hardening during plastic deformation under monotonic loading is proposed. For this purpose, the anisotropic plastic potential coefficients are assumed to be functions of a measure of the accumulated plastic strain. This model is applied to describe the plastic behavior of a magnesium alloy (ZM21) sheet at room temperature. The selected plastic potential accounts for the main features of Mg alloy plasticity, i.e., anisotropy and strength-differential (SD) effects. All the accumulated plastic strain dependent coefficients of the phenomenological model are determined from input data generated with a crystal plasticity approach. They are optimized to best capture the accumulated strain dependent potentials computed with crystal plasticity. The R-value (Lankford coefficient) anisotropy is used as an independent measure for the assessment of the approximation quality. This model is implemented into a finite element (FE) code and successfully validated through the numerical simulations of the cup drawing test. The calculated earing profile obtained with the proposed hardening model is compared to results assuming isotropic hardening for various plausible shapes of the plastic potential. Although the ear and valley numbers and positions are similar in all cases, the height differences

between peaks and valleys are strongly dependent on the type of constitutive approach used in the simulation.

**Keywords** Finite elements · Anisotropy · Plasticity · Strength differential effect · Parameter identification

## Introduction

Magnesium alloys have attracted attention in recent years as lightweight materials for the transportation industry. Indeed, the low density of magnesium and its relatively high specific strength make it an excellent candidate for applications in transportation industries, where saving of structural weight and reduction of fuel consumption are common challenges. A broad application of wrought magnesium alloys in modern vehicles and consumer goods requires reliable simulation tools for predicting the forming capabilities, the structural behavior under mechanical loads and the lifetime of the component. The respective constitutive models have to account for several peculiarities of the mechanical behavior: Its pronounced strength differential effect (different yield strength in tension and compression) at low homologous temperatures and its strong deformation anisotropy [1, 2]. Both demand for non state-of-the-art simulation techniques.

The mechanical behavior of metals with hexagonal closed packed (hcp) crystal structure differs considerably from that of metals with fcc and bcc crystal structures. Due to the low-symmetry of the crystal, independent slip systems necessary for plastic deformation are not easily activated at room temperature. Hence, twinning occurs as an alternate deformation mechanism. In general, the limited amount of slip systems limit ductility and formability [3]. Rolled magnesium sheets usually show a strong basal texture, and therefore exhibit the mentioned mechanical properties.

---

D. Steglich (✉) · J. Bohlen  
GKSS Forschungszentrum Geesthacht,  
Institute of Materials Research, Materials Mechanics,  
Geesthacht, Germany  
e-mail: dirk.steglich@gkss.de

W. Brocks  
Technical Faculty of Christian-Albrechts-University,  
Kiel, Germany

D. Steglich · F. Barlat  
G.I.F.T., Pohang University of Science and Technology,  
Pohang, Korea

Crystal plasticity provides an appropriate tool for studying these phenomena on a micro-scale [4–8]. This approach requires detailed information on the local deformation mechanisms and the respective constitutive properties as well as on the distribution of crystallographic orientations of individual grains resulting from texture. Crystal plasticity (CP) is an adequate model for understanding the micro-mechanisms of plastic deformations in hcp metals and for predicting their macroscopic properties [9]. However, for computation time considerations, it is obviously an improper approach to be applied for real-part forming simulations. The latter requires phenomenological modelling in the framework of continuum mechanics and the finite element (FE) method. Following the work of Graff et al. [9], the description of yield surfaces for magnesium as proposed by Cazacu and Barlat [10] has been adopted and extended with respect to a phenomenological description of direction-dependent hardening.

**Constitutive behavior**

Anisotropy and strength differential effect in plasticity

Constituent elements of any theory of plasticity are the yield condition, the flow rule and hardening laws. The yield condition

$$\varphi(\sigma_{ij}) = 0, \tag{1}$$

separates purely elastic from elasto-plastic states, where  $\varphi(\sigma_{ij}) \leq 0$  is the yield function or plastic potential in the case of an associated flow rule. For isotropic, pressure insensitive materials, the yield function must not depend on the choice of the coordinate system. This implies that it may depend on the 2nd and 3rd principal invariant of the deviatoric stresses,

$$\begin{aligned} J_2(\sigma'_{ij}) &= \frac{1}{2}(\sigma'_{ik}\sigma'_{ki}) \\ J_3(\sigma'_{ij}) &= \det(\sigma'_{ij}) = \frac{1}{3}\sigma'_{ij}\sigma'_{jk}\sigma'_{ki} \end{aligned} \tag{2}$$

only. A particular phenomenon, namely the asymmetry of the yield surface with respect to tension and compression

(strength differential effect), can be captured by means of the  $J_3$ . If the yield condition is an even function of the principal stresses, the yield stresses in tension and compression are equal. Tension-compression asymmetry can be captured using

$$\varphi(J_2^{3/2} - cJ_3) = \tau_Y^3 \tag{3}$$

[10, 11], where  $\tau_Y$  is the shear yield stress and the range of the coefficient  $c$  is limited by the convexity condition.

The changes of the yield surface with loading history is addressed as hardening and generally described by scalar and tensorial internal variables, which follow specific evolution laws. Commonly, the number of internal variables is restricted to two, namely the accumulated (equivalent) plastic strain,

$$\bar{\epsilon}^p = \int_0^t \dot{\bar{\epsilon}}^p d\tau, \tag{4}$$

and the deviatoric back stress tensor. The latter will not be considered here.

Anisotropic yielding requires the appropriate modification of the equivalent stress, which of course will not be invariant with respect to an arbitrary rotation of the coordinate system any more but only with respect to the specific material symmetry axes. The model proposed by Cazacu and Barlat [10], developed in the frame of the tensor representation approach, captures orthotropy as well as asymmetry in yielding in pressure-insensitive metals by generalisations of the second and third deviatoric invariants,  $J_2$  and  $J_3$ :

$$(J_2^{\text{orth}})^{3/2} - cJ_3^{\text{orth}} - \tau_Y^3 = 0. \tag{5}$$

Here,  $\tau_Y$  is some fictitious yield strength in shear. The generalisations of  $J_2$  and  $J_3$  to orthotropy are given by

$$\begin{aligned} J_2^{\text{orth}} &= \frac{1}{6} [a_1(\sigma_{11} - \sigma_{22})^2 + a_2(\sigma_{22} - \sigma_{33})^2 + a_3(\sigma_{33} - \sigma_{11})^2] \\ &\quad + 3(a_4\sigma_{12} + a_5\sigma_{23} + a_6\sigma_{13}) \end{aligned} \tag{6}$$

$$\begin{aligned} J_3^{\text{orth}} &= \frac{1}{27}(b_1 + b_2)\sigma_{11}^3 + \frac{1}{27}(b_3 + b_4)\sigma_{22}^3 + \frac{1}{27}[2(b_1 + b_4) - (b_2 + b_3)]\sigma_{33}^3 + \\ &\quad - \frac{1}{9}(b_1\sigma_{22} + b_2\sigma_{33})\sigma_{11}^2 - \frac{1}{9}(b_3\sigma_{33} + b_4\sigma_{11})\sigma_{22}^2 - \\ &\quad - \frac{1}{9}[(b_1 - b_2 + b_4)\sigma_{11} + (b_1 - b_3 + b_4)\sigma_{22}]\sigma_{33}^2 + \frac{2}{9}(b_1 + b_4)\sigma_{11}\sigma_{22}\sigma_{33} + \\ &\quad + \frac{1}{3}[(2b_{10} - b_5)\sigma_{11} + b_5\sigma_{22} - 2b_{10}\sigma_{33}]\sigma_{12}^2 + \\ &\quad + \frac{1}{3}[-(b_6 + b_7)\sigma_{11} + b_6\sigma_{22} + b_7\sigma_{33}]\sigma_{23}^2 + \\ &\quad + \frac{1}{3}[(2b_9 - b_8)\sigma_{11} - 2b_9\sigma_{22} + b_8\sigma_{33}]\sigma_{13}^2 + 2b_{11}\sigma_{12}\sigma_{23}\sigma_{13}, \end{aligned} \tag{7}$$

with  $a_i$  and  $b_i$  being (constant) model parameters. The yield strength in shear,  $\tau_Y$ , is related to a respective uniaxial tensile strength,  $\sigma_Y$ , of a fictitious isotropic material by

$$\tau_Y = \left( \frac{3\sqrt{3} - 2c}{27} \right)^{1/3} \sigma_Y, \tag{8}$$

allowing to write the yield condition (5) as a function of a “uniaxial” stress measure,  $\sigma_Y$  [10]. Without loss of generality, the constant  $c$  in Eq. 8 may be set equal to 1, resulting in corresponding changes of the constants  $b_i$ .

The associated flow rule obviously becomes complicated by the introduction of  $J_3$ , and no explicit equivalent plastic strain rate,  $\dot{\bar{\epsilon}}^p$ , meeting the postulate of equivalence of dissipation rates,

$$\dot{W}^p = \sigma_{ij} \dot{\epsilon}_{ij}^p = \bar{\sigma} \dot{\bar{\epsilon}}^p, \tag{9}$$

has yet been derived for this case. A respective definition would include the anisotropy parameters  $a_i$  and  $b_i$ , and as these parameters are assumed as evolving with plastic deformation, later on, the definition would depend on the load history. This does not appear as feasible. Hence, for the sake of simplicity the definition associated to von Mises’ yield condition

$$\dot{\bar{\epsilon}}^p = \sqrt{\frac{2}{3} \dot{\epsilon}_{ij}^p \dot{\epsilon}_{ij}^p} \tag{10}$$

is adopted in the following, though this obviously conflicts with Eq. 9.

### Strain hardening

If hardening is assumed to be purely isotropic, the yield surface expands in a self-similar way depending on  $\bar{\epsilon}^p$ . Textured hcp alloys have a rather peculiar hardening behavior, however, which is due to twinning inducing grain reorientation, creation and disappearance of twin boundaries. Both experimental investigations of Kelley and Hosford [12] on pure magnesium and numerical studies based on crystal plasticity by Graff et al. [9] indicate that not only the position and the dimension but also the shape of the stress isocontours at constant accumulated plastic strain evolve with deformation, which would require a dependence of the orthotropy parameters on the plastic strain. Lee et al. [13] proposed a two-surface theory for magnesium alloy sheets accounting for anisotropy by means of a linear transformation of the stress deviator and the strength differential effect by introducing a kinematic hardening concept.

Cazacu and Barlat [10] fitted their model to the experimental results of Kelley and Hosford [2] in dependence on plastic strain,  $a_i(\bar{\epsilon}^p)$  and  $b_i(\bar{\epsilon}^p)$ , but they did not establish any evolution law for strain hardening. Application of their model to forming simulations necessitates an extrapolation for higher strains. A respective enhancement of their model has been proposed by Ertürk et al. [14, 15], which includes strain-rate and temperature dependent behavior. Discarding the two latter effects, the modified invariants in Eq. 5 are taken as dependent on the accumulated plastic strain,  $\bar{\epsilon}^p$ , only:

$$(J_2^{\text{orth}}(\bar{\epsilon}^p))^{3/2} - J_3^{\text{orth}}(\bar{\epsilon}^p) = \tau_Y^3(\bar{\epsilon}^p). \tag{11}$$

The right hand side can be related to the uniaxial stress–strain curve in tension, thus  $\tau_Y^3(\bar{\epsilon}^p)$  acts as a “fictitious” reference curve. Saturating exponential functions are assumed for the parameters of orthotropy,

$$\begin{aligned} a_i &= A_i^{(a)} + B_i^{(a)} \left( 1 - \exp\left(-C_i^{(a)} \bar{\epsilon}^p\right) \right) \\ b_i &= A_i^{(b)} + B_i^{(b)} \left( 1 - \exp\left(-C_i^{(b)} \bar{\epsilon}^p\right) \right) \end{aligned} \tag{12}$$

Equations 11 and 12 depend solely on the plastic equivalent strain as an internal variable. This limits the application of the constitutive model to monotonic loading paths. Neither load path changes nor load reversals may be described properly. However, for monotonic paths it is assured that, through the exponential functions, the material tends towards a steady state behavior. Together with the definitions of the second and third invariant of the stress deviator, Eqs. 6 and 7, this yield condition and its associated flow rule is able to describe material anisotropy and direction-dependent hardening.

This model in its tri-dimensional formulation has been implemented into the commercial finite element code ABAQUS via the user interface UMAT [16]. All following simulations have been carried out using ABAQUS/Standard.

### Reduction to 2D

The two invariants in Eq. 5,  $J_2^{\text{orth}}$  and  $J_3^{\text{orth}}$ , contain a total of 17 coefficients in the 3D representation, namely six  $a_i$  and eleven  $b_i$ . The constant  $c$  is set equal to 1. The number of coefficients reduces for 2D cases like plane stress or axisymmetric states.

Assuming a plane stress state in the {1,2}-plane,  $\sigma_{33} = \sigma_{13} = \sigma_{23} = 0$ , results in

$$\begin{aligned} J_2^{\text{orth}(12)} &= \frac{1}{6} \left[ a_1(\sigma_{11} - \sigma_{22})^2 + a_2\sigma_{22}^2 + a_3\sigma_{11}^2 \right] + a_4\sigma_{12}^2 \\ J_3^{\text{orth}(12)} &= \frac{1}{27}(b_1 + b_2)\sigma_{11}^3 + \frac{1}{27}(b_3 + b_4)\sigma_{22}^3 - \frac{1}{9}b_1\sigma_{22}\sigma_{11}^2 - \frac{1}{9}b_4\sigma_{11}\sigma_{22}^2 + \\ &\quad + \frac{1}{3}[(2b_{10} - b_5)\sigma_{11} + b_5\sigma_{22}]\sigma_{12}^2 \end{aligned} \tag{13}$$

that is ten material coefficients,  $a_1, a_2, a_3, a_4, b_1, b_2, b_3, b_4, b_5, b_{10}$ . If  $\{1,2\}$  are principal axes, the shear stress vanishes,  $\sigma_{12}=0$ , and  $a_4, b_5, b_{10}$  remain indeterminate.

Since a biaxial test is not very convenient for parameter identification, uniaxial and homogeneous stress states as approximately achieved in tension or compression test samples can be considered. Tension or compression in (1)-direction,  $\sigma_{22}=0$ , yields

$$J_2^{\text{orth}(1)} = \frac{1}{6}(a_1 + a_3)\sigma_{11}^2, \quad (14)$$

$$J_3^{\text{orth}(1)} = \frac{1}{27}(b_1 + b_2)\sigma_{11}^3,$$

and in (2)-direction,  $\sigma_{11}=0$ ,

$$J_2^{\text{orth}(2)} = \frac{1}{6}(a_1 + a_2)\sigma_{22}^2, \quad (15)$$

$$J_3^{\text{orth}(2)} = \frac{1}{27}(b_3 + b_4)\sigma_{22}^3.$$

A total of seven coefficients,  $a_1, a_2, a_3, b_1, b_2, b_3, b_4$ , as in the biaxial plane stress with  $\sigma_{12}=0$ , are involved. Four tests do not suffice, however, to determine seven coefficients if no additional information is provided, for instance on a ratio of (plastic) strains or on pure shear load.

## Polycrystalline representative volume elements

### Material and microstructure

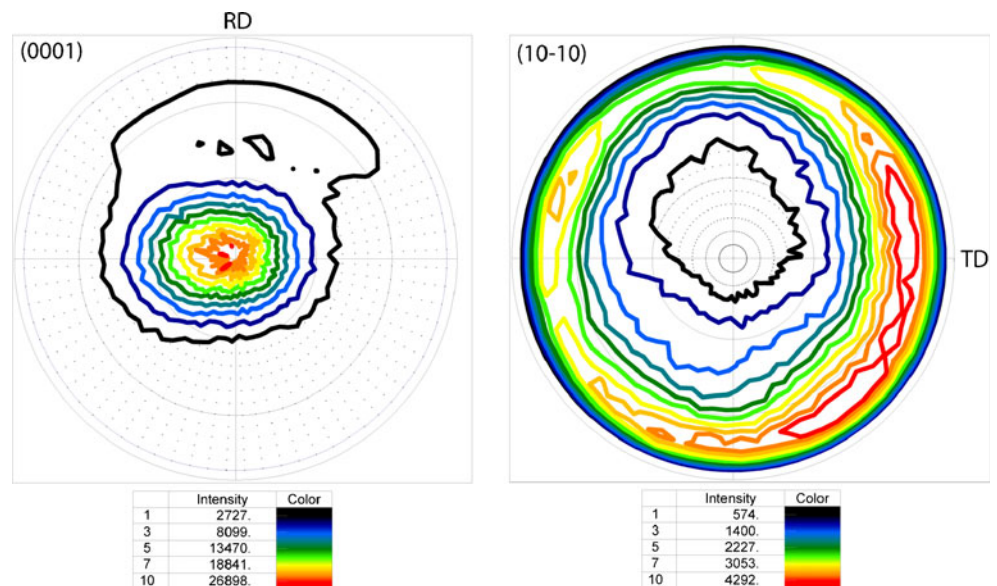
As a model material a rolled sheet of the magnesium alloy ZM21 (containing 2.1 wt% zinc and 0.8 wt% manganese) is considered. Texture measurements have been conducted and recalculated pole figures (see Fig. 1) evidence the distribution of the basal planes which are mainly orientated in the sheet plane and show a distinctive angular distribu-

tion towards rolling direction and a smaller angular distribution towards the transverse direction [17]. The texture information was mapped to the prescribed number of crystal orientations (i.e. number of finite elements in the RVE) following the method of Toth and van Houtte [18]. Each crystal was assumed to obey the same visco-plastic response (crystal plasticity, CP) [5, 19, 20]. Slip and twinning mechanisms, hardening characteristics and self- and latent hardening parameters have been adopted from [9, 21, 22], however, the resolved shear stresses have been adjusted to approximately meet the uniaxial stress–strain curve of the material in rolling and transverse direction.

### Biaxial loading of RVEs

Phenomenological constitutive equations for yielding and hardening under multiaxial stress states are usually established on a macroscopic level. In modeling of the micro-mechanisms, in contrast, special emphasis is put on the quantitative description of physical deformation mechanisms. The transfer from the micro- to the macroscale can be performed by the analysis of representative volume elements (RVEs), which are designed to represent typical periodic microstructures of a polycrystalline material. The constitutive equations are then those of crystal plasticity, where slip is assumed to act on specific planes and obeys Schmid's law. By this means, the effect of texture on the global deformation behavior can be investigated numerically. For biaxially loaded RVEs ( $\{1,2\}$ -plane is assumed to be equivalent to the  $\{L,T\}$ -plane), contours of constant plastic work can be computed from the applied stresses and resulting plastic strains using relation (9). These numerically generated iso-contours have hence to be fitted by an analytical expression of the plastic potential and an

**Fig. 1** Recalculated basal and prismatic pole figures of Mg ZM21 in the as received condition



evolution equation for this yield potential can be established. For practical reasons (hardening is commonly expressed as a function of strain), however, contours of constant plastic accumulated strain will be later used in this work.

The iterative identification procedure for the parameters of the phenomenological model is illustrated in Fig. 2. Crystal plasticity parameters calibrated for pure magnesium [9] are considered as a starting point. As the slip system activity is affected by alloying elements it is expected that the parameters have to be changed in order to meet the behaviour of the technical alloy considered here. Like in the aforementioned paper, the deformation twinning mechanism is handled as additional slip mechanisms of the type  $\{10\bar{1}2\}\langle 10\bar{1}1 \rangle$  and the reorientation of crystallographic planes due to rotation is not taken into account. This way of representation for twinning assumes that, as twinning has saturated, further plastic deformation issues only in the “untwinned” material. Furthermore, it is assumed that both slip and twinning can operate simultaneously at a material point. Deformation twinning modeled as crystallographic slip is supposed to follow Schmid’s law. The polar character of twinning is taken into account with the restriction for the resolves shear stresses,

$$\tau_Y^{(\alpha)} \rightarrow \infty \quad \text{for} \quad \tau^{(\alpha)} \leq 0, \tag{16}$$

allowing extension of the *c*-orientation (tensile twinning) only.

Tensile tests using the RVE described earlier in RD and TD are simulated and the respective results are compared with experimental results, see Fig. 3. To obtain agreement between tests and simulations, the CP parameters have been adjusted. On the basis of these parameters the simulations of the biaxially loaded polycrystalline aggregates have been conducted.

These RVEs are modeled by  $12^3$  fully integrated quadratic brick finite elements representing the equivalent number of grains. Each grain is attributed a specific

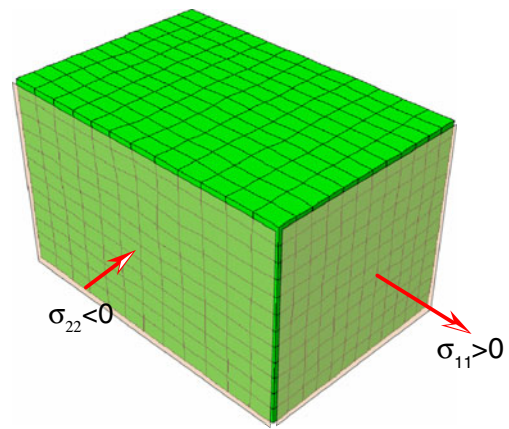
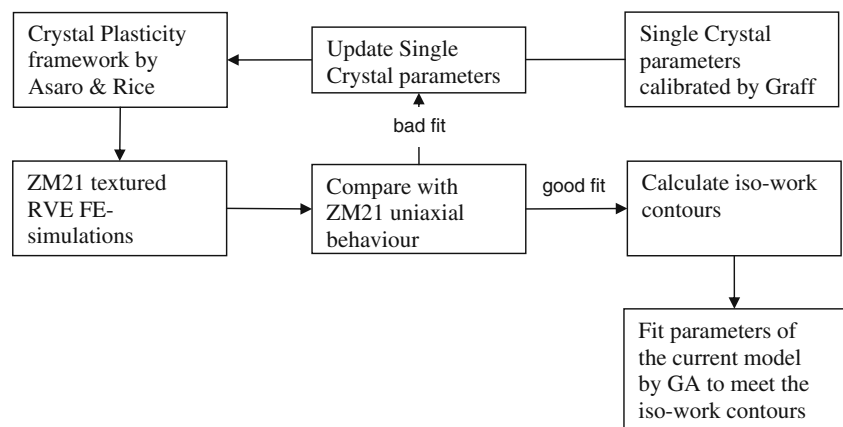


**Fig. 3** Volume element representing a textured polycrystal consisting of  $12 \times 12 \times 12$  grains under biaxial load

crystallographic orientation and the distribution of these orientations in space represents the texture of the aggregate. The RVE is constrained to have straight and perpendicular faces in order to ensure the microstructure’s periodicity. In order to retrieve information about the yielding behavior, radial loading paths are analyzed spanning the whole space of biaxial principal stresses. A schematic of the microstructural model is shown in Fig. 4, indicating that the “mesoscopic” stresses  $\sigma_{11}$  and  $\sigma_{22}$  are applied on the faces of the cube. Figure 5 displays a typical mechanical response of RVE visualized in stress space for given (prescribed) values of specific plastic work. It reveals the initial asymmetry in tension and compression, which becomes less pronounced once the applied load increases (i.e., at higher values of plastic work). In the initial stage of loading the iso-work contours are smooth convex curves. For higher values of plastic work, however, the contours’ shape become more and more “hexagonal”, showing a similar appearance than the well known Tresca yield criterion.

In the following, the mechanical response of the RVE is displayed showing contours of plastic equivalent strain instead of plastic work. Although mechanically less

**Fig. 2** Flowchart of the parameter fitting procedure for the proposed model



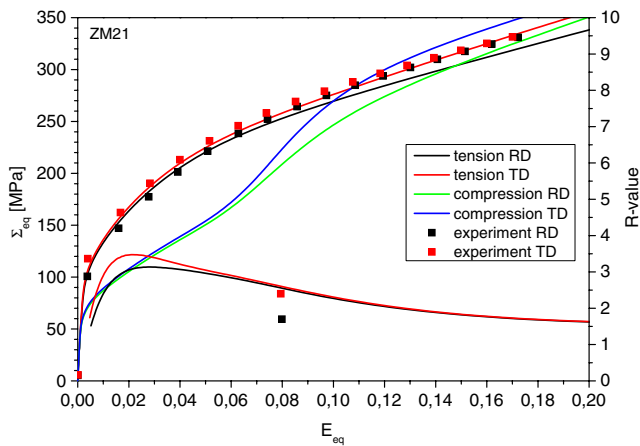


**Fig. 4** Mechanical test results of the material under investigation (symbols) compared to the RVE simulation results (lines). Compression tests are not available

significant, the first has the advantage that comparison with the respective contours derived from Eq. 11 can be done easily.

**Optimisation procedure**

The parameter identification is accomplished by an optimisation procedure minimising the differences between given (or prescribed) values and the yield function of the model, Eq. 11, which are quantified by some objective function

$$\Psi = \sum_m \sum_n \left[ \sigma_{Y,mod}^{(n)}(\varepsilon_m^p) - \sigma_{Y,exp}^{(n)}(\varepsilon_m^p) \right]^2 \Rightarrow \min, \quad (17)$$

where  $n=1, \dots, N$  indicates the yield stresses in the  $N$  radial loading directions, and  $m$  discrete values of plastic strain. The optimisation procedure is based on a genetic algorithm [23] and has to account for some constraint conditions:

- The yield strength in shear has to be a positive increasing function of plastic strain resulting in

$$(J_2^{orth})^{3/2} - J_3^{orth} \geq 0, \quad (18)$$

- In order to ensure convexity of the yield surface, the Hessian matrix of the yield function

$$\underline{H} = \begin{pmatrix} \frac{\partial^2 \phi}{\partial \sigma_{11}^2} & \frac{\partial^2 \phi}{\partial \sigma_{11} \partial \sigma_{22}} \\ \frac{\partial^2 \phi}{\partial \sigma_{11} \partial \sigma_{22}} & \frac{\partial^2 \phi}{\partial \sigma_{22}^2} \end{pmatrix}, \quad (19)$$

must be positive semi-definite, i.e.

$$\begin{aligned} H_{11} &\geq 0 \quad (\text{or } H_{22} \geq 0) \\ H_{11}H_{22} - H_{12}^2 &\geq 0 \end{aligned}, \quad (20)$$

- The iso-strain contours representing the yield loci of a hardening material in the stress plane are supposed to evolve without intersecting.

The last two side conditions can only be proven for discrete stages of deformation. In the algorithm, the number of tested stages has been chosen to be very high. Consequently, convexity and intersection-free evolution are satisfied with a high probability, but no general proof can be provided.

The yield strength in shear,  $\tau_Y(\bar{\varepsilon}^p)$ , has in the present case been calculated from the tensile stress in L-direction,  $\sigma_Y^{L,ten}(\bar{\varepsilon}^p)$ , according to

$$\tau_Y = \left( \left[ \frac{1}{6}(a_1 + a_2) \right]^{3/2} - \frac{1}{27}c(b_3 + b_4) \right)^{1/3} \sigma_Y^{L,ten}. \quad (21)$$

Provided that the hardening  $\sigma_Y^{L,ten}(\bar{\varepsilon}^p)$  can be taken directly from the response of the RVE, Eq. 21 cannot be directly solved for  $\tau_Y$  because it includes functions dependent on  $\bar{\varepsilon}^p$ , see Eq. 12. In order to retrieve the uniaxial behavior, an additional side condition has been introduced, which guarantees that the optimised yield functions intersect the positive  $\sigma_1$ -axis at exactly the same points than the response of the RVE.

**Optimisation results**

Two different optimisation routes are considered in the following. The first one aims at meeting only one contour of plastic work, and fitting constant parameters  $a_1, a_2, a_3, b_1, b_2, b_3, b_4$  for the plastic potential from the virtual biaxial tests. This is similar to the procedure used in [24]. The second route aims on meeting several contours at the same time, which requires the use of Eq. 12 leading to  $7 \times 3 = 21$

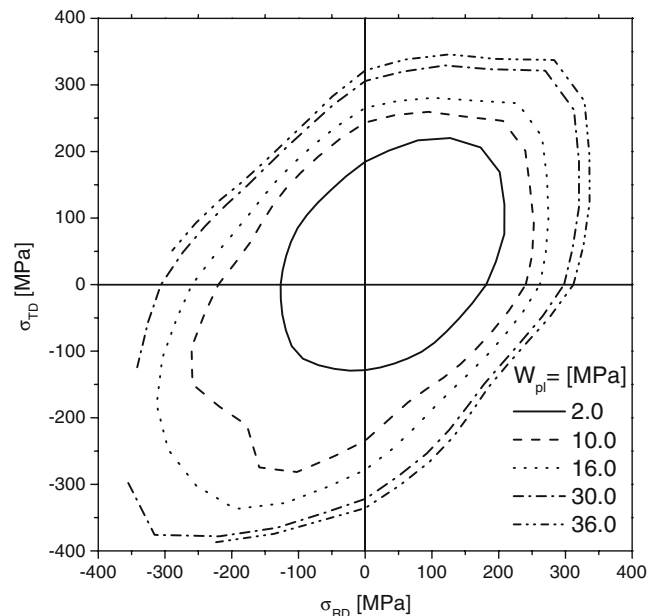


**Fig. 5** Contours of constant specific plastic work obtained from radial loading paths

parameters. The reference curve, right hand side of Eq. 11, is assumed to be the same in both cases. The parameters used in the simulations are summarised in Table 1.

It has to be mentioned here that three more coefficients,  $a_4, b_5, b_{10}$ , are physically relevant in plane stress and hence influence the result for arbitrary mechanical loading situations. As already pointed out they cannot be determined from the suggested tests and therefore have to be preset to “reasonable” values.

Figure 6 shows the optimisation result if only one contour is considered:  $\bar{\epsilon}^p = 0.02, \bar{\epsilon}^p = 0.08, \text{ or } \bar{\epsilon}^p = 0.14$  leading to set#1, set#2 or set#3, respectively (see Table 1). Obviously each of the contours is met very well. Their respective shapes differ significantly from the one of the von Mises ellipse (included in the figure for comparison). In any 3D-simulation, one of these sets of parameters can be used together with an isotropic hardening function in principle. However, it is then not possible to account for the change of the contours shape.

In Fig. 7 the effect of the different parameter sets on the R-value

$$R = \frac{\epsilon_w^{pl}}{\epsilon_t^{pl}} \tag{22}$$

obtained from tensile tests conducted in different directions  $\varphi \in [0^\circ, 90^\circ]$  from rolling direction ( $\varphi=0^\circ$ ) is depicted.  $\epsilon_w^{pl}$  and  $\epsilon_t^{pl}$  refer to the plastic strains in the width and thickness directions of the tensile specimen. The respective R-values can either be calculated from the plastic potential using the normality rule or extracted from finite element simulations directly by monitoring the strains and using Eq. 22. The latter procedure was used here.

**Table 1** Model parameters used in the FE-simulations; <sup>(a)</sup> indicates values which remain undetermined by the optimisation procedure

3D	Plane stress	Set#1 (0.02)	Set#2 (0.08)	Set#3 (0.14)	Set#4 ( $A^{(a,b)}, B^{(a,b)}, C^{(a,b)}$ ) <sub>i</sub>
$a_1$	$a_1$	0.0558	2.0389	2.8938	0.9476, 1.9429, 1.9300
$a_2$	$a_2$	3.3594	2.7276	2.9709	1.2250, 1.3538, 0.5979
$a_3$	$a_3$	3.2525	3.2151	3.5400	1.2885, 1.5705, 1.9199
$a_4$	$a_4$ <sup>(a)</sup>	4	4	4	4, 0, 0
$a_5$	–	1	1	1	1, 0, 0
$a_6$	–	1	1	1	1, 0, 0
$b_1$	$b_1$	–2.413	–1.0642	2.7874	0.0476, 2.5859, 0.1498
$b_2$	$b_2$	9.0126	7.3961	0.8993	2.3522, 0.2891, 0.7923
$b_3$	$b_3$	8.6030	1.4114	–0.4659	1.2332, 0.4304, 2.5065
$b_4$	$b_4$	–2.4071	–0.3435	–0.1422	0.0511, 3.5625, 1.8850
$b_5$	$b_5$ <sup>(a)</sup>	1.5	1.5	1.5	1.5, 0, 0
$b_6$	–	1	1	1	1, 0, 0
$b_7$	–	1	1	1	1, 0, 0
$b_8$	–	1	1	1	1, 0, 0
$b_9$	–	1	1	1	1, 0, 0
$b_{10}$	$b_{10}$ <sup>(a)</sup>	3	3	3	3, 0, 0
$b_{11}$	–	1	1	1	1, 0, 0

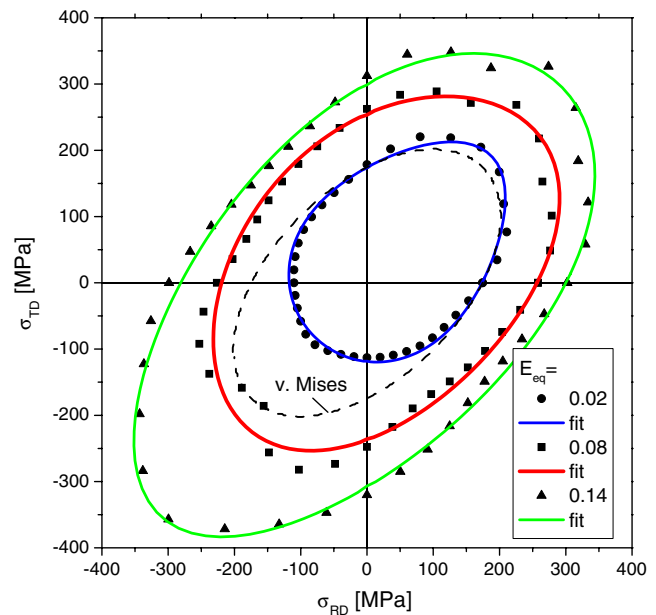


**Fig. 6** Fit of CP data using the yield function Eq. 5 by three independent sets of constant parameters ( $a_i, b_i$ ) at plastic equivalent strains of 0.02, 0.08 and 0.14

Typically for rolled magnesium alloys the R-value is higher than one. This is due to the strong basal texture and the limited amount of slip systems acting in the thickness direction. The variation of the R-value with respect to the loading direction for each stress level is large, in particular for the first stress level which corresponds to the onset of yielding. While hardening takes place, the overall level of R-value decreases and its variation decreases as well. This appears to be physically sound, because at high strains the initial (basal)

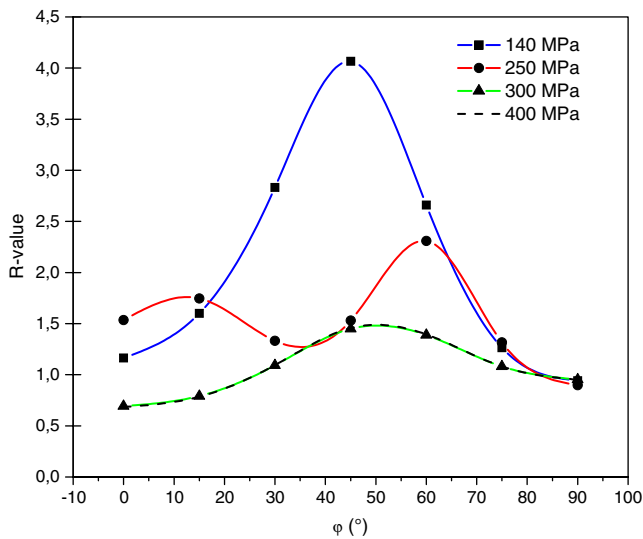


**Fig. 7** Orientation-dependence of the R-value at different stress levels, namely 140, 250, 300 and 400 MPa (correspond approximately to levels of plastic strain 0.02, 0.08, 0.14 and 0.2)

texture may change and accommodate more easily deformation in the sheet thickness direction. The black dashed line in Fig. 7 represents an extrapolation, as the respective contour is not included in Fig. 6. In this case, the last contour is expanded due to pure isotropic hardening, and no shape change is associated. However, it has to be emphasized in this example there is no continuous transition for one to the other optimised contours, i.e. set of model parameters.

This can be overcome by using the second optimisation strategy, which is shown in Fig. 8. In this case in total seven contours  $\bar{\epsilon}^p=0.02, 0.04, 0.06, 0.08, 0.1, 0.12, 0.14$  were

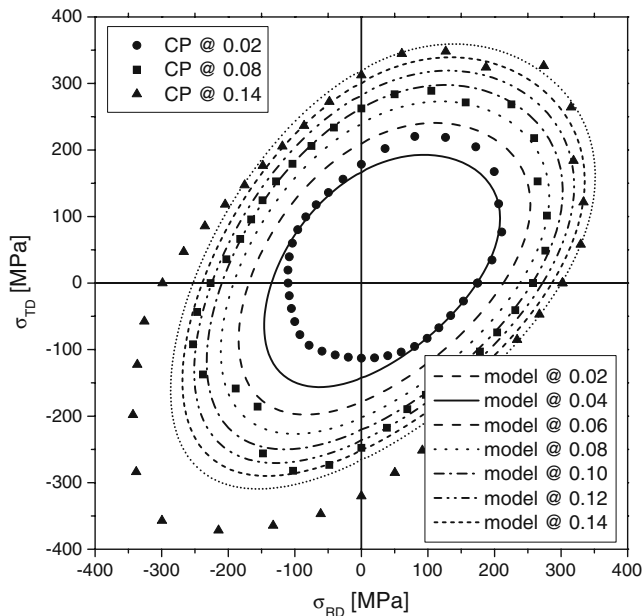


**Fig. 8** Fit of CP data using the yield function Eq. 11 using variable parameters ( $a_i, b_i$ ) following Eq. 12

included in the objective function to find the 27 parameters  $A_i, B_i$  and  $C_i$ . The obtained fit seems to be reasonable, in particular for the intermediate contours. In case of the inner contour, however, the typical tension-compression asymmetry is underestimated, whereas for the outer contours it is overestimated. As several optimisation trials have been carried out, it seems that meeting all prescribed contours ideally is impossible with the ansatz used. In this context, the result shown in Fig. 8 represents a reasonable set, worth being investigated in detail. It is worth to mention here that this particular result does not pass through the data obtained by independent fits at 0.02, 0.08 and 0.14 shown in Fig. 6. This is due to the optimisation procedure, which aims on an overall fit instead on a fit at discrete strain levels.

The resulting variation of the R-value is less pronounced compared to the previous case. Especially at stresses close to the first yield stress the variation is more realistic, as the maximum is close to 2.1. The general shape of the curve is maintained even at higher stresses, which reveals that the change of shape between the different contours in Fig. 8 is small. The curve in Fig. 9 marked by triangles represents an extrapolation, as data for this stress level have not been incorporated in the objective function. The difference between the curve for 300 MPa and 400 MPa indicates that still in this regime small shape changes of the contours appear, as the exponential functions, Eq. 12, are not saturated.

### Application to cup-drawing

Forming simulations have been carried out for parameter sets obtained from the two different optimisation routes.

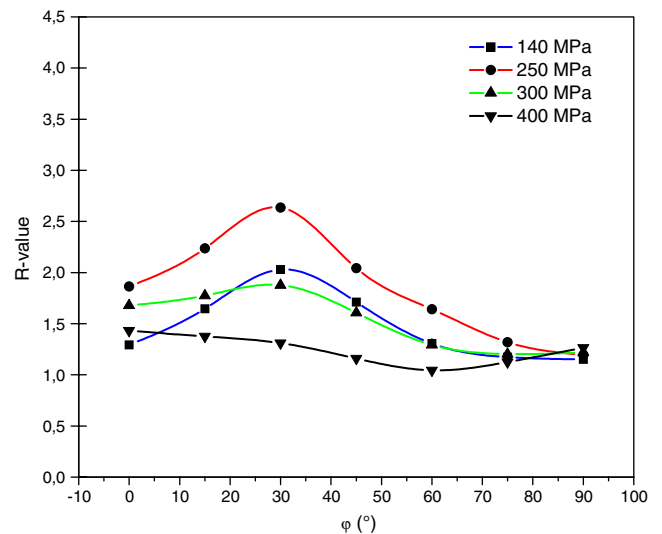


**Fig. 9** Variation of the orientation-dependent R-value with increasing hardening

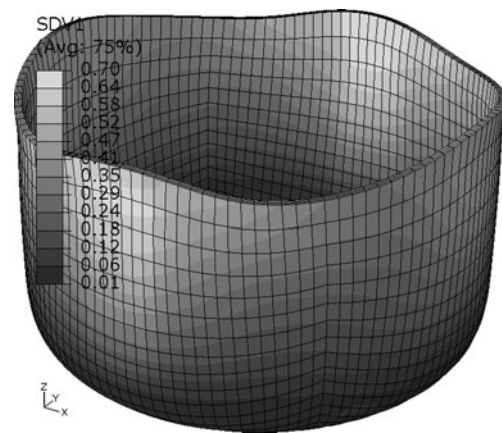


The FE-model represents a typical cup-drawing experiment used in various experimental and numerical studies, e. g. [25]: A circular blank of radius  $r$  is formed through a rigid punch, die and holder to a cylindrical cup. Because of the complicated stress states which appear during cup drawing, this process can be used for the study of sheets' structural responses depending on its mechanical properties.

Punch, die and holder have been modelled in this case as rigid surfaces. The blank consists of a disc with two or four layers of fully integrated 8-noded 3D brick finite elements (linear displacement functions) in the thickness direction. Between sheet and die, sheet and punch and sheet and holder, tangential forces can be transmitted following Coulomb's law of friction with a coefficient of 0.05. The model parameters used of the different simulation runs are summarized in Table 1. Parameters associated with the stresses in sheet's thickness direction are physically not relevant, as the thickness stress usually can be neglected. However, they have to be provided in the 3D-model and thus were set to 1 throughout the simulations.

Figure 10 shows the simulation results at the end of the respective forming process in the case of the three independent plastic potentials each undergoing pure isotropic hardening. Contours of constant plastic equivalent strain are displayed. All cups exhibit pronounced earing profiles. In case of the plastic potential calibrated using the  $\bar{\epsilon}^p = 0.02$ —contour (see Fig. 10a) it is most significant. This is due to the strong change of the R-value, see Fig. 7. As the variations on the R-value decrease from  $\bar{\epsilon}^p = 0.08$ —contour to  $\bar{\epsilon}^p = 0.14$ —contour, the height of the “ears” after forming decreases accordingly.

Figure 11 finally shows the result of the forming simulation using the continuous formulation of the yield function parameters, Eq. 12. As expected from Fig. 10, the earing is less pronounced than in the previous cases. For quantitative comparison of the different earing profiles, the cup's height normalized by the initial radius of the sheet is plotted as a function of the circumferential coordinate in



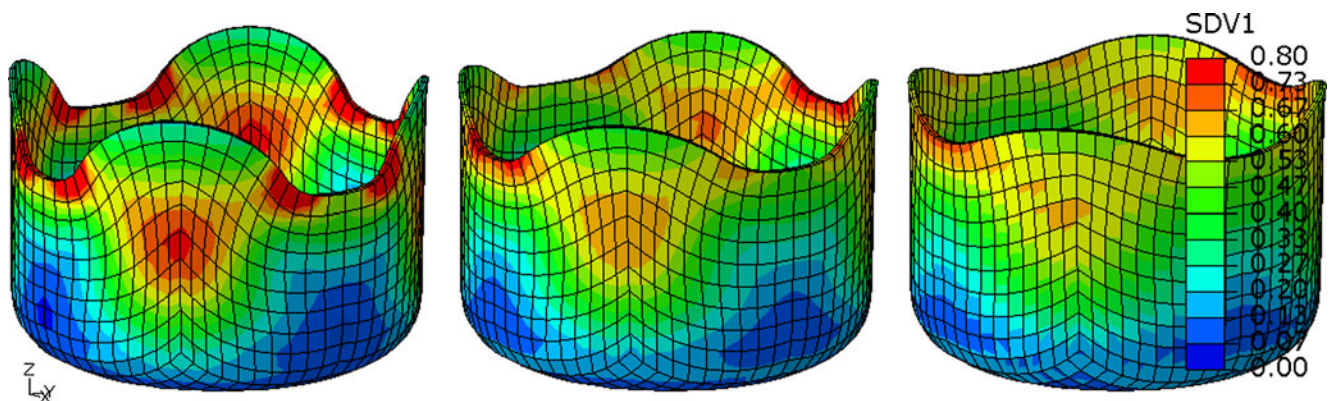
**Fig. 11** Results of the cup drawing simulation using the parameter set #4 represented in Fig. 5, contours of constant plastic equivalent strain are shown

Fig. 12. The visual impressions of Figs. 10 and 11 are confirmed—the earing is most pronounced in case of the set#1 and less pronounced in case of set#4. Although significant differences exist between the parameter sets, the number of ears and their position with respect to the axes of orthotropy is the same in all cases: The cups height is maximum under  $45^\circ$  from the rolling direction, leading to four ears in total.

**Discussion and conclusions**

The simulations of cup drawing experiments confirm that a complex forming operation can be described by the proposed model. The side conditions of convexity and non-intersection of subsequent contours of plastic work are satisfied, leading to a stable and convergent numerical solution. This should allow using this approach on a phenomenological level.

A calibration of the model parameters via RVE simulations using crystal plasticity models can be conducted if no multi-axial experiments are available, but of course this



**Fig. 10** Results of the cup drawing simulation using pure isotropic hardening and different sets of constant parameters for the yield functions (0.02, 0.08 and 0.14 in Fig. 3), contours of constant plastic equivalent strain are shown

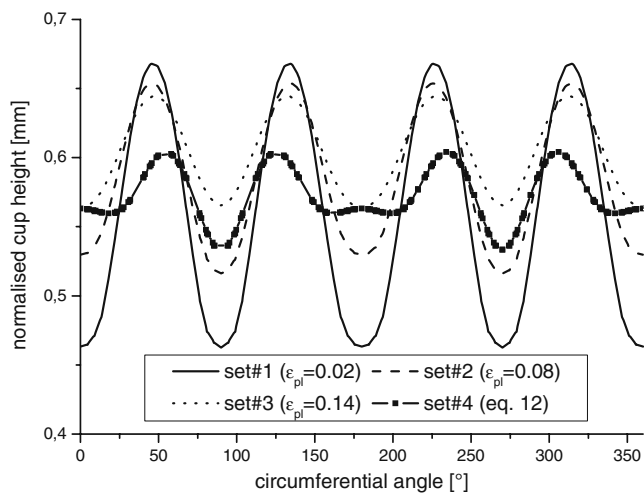


**Fig. 12** Circumferential distribution of the normalized cups rim height after forming. 0° and 90° correspond to rolling and transverse directions, respectively

shifts the problem to finding meaningful quantities of resolved shear stresses, hardening characteristics and interactions of slip systems. The fit obtained in the present contribution appears not to be perfect once one focuses on the stress level at prescribed values of plastic strain exclusively, see Figs. 6 and 8. But the tendency of the R-value to decrease with increasing strain is met by the model, see Fig. 9. R-value-variations are used here to study the model response in *tension*. As the model includes the third invariant of the stress deviator, the respective variation in *compression* is expected to be different. However, because this information is not used for the calibration process, respective predictions are not shown here.

A fundamental question is the significance of the dataset used for the model calibration. The current approach aims on the description of distortional hardening in general, and the authors are well aware of the fact that the solution provided is not unique.

As already mentioned earlier, three of the total 10 parameters involved in the yield function could not be determined by the procedure used here. They are related to shear stresses, which are zero for the radial loading paths considered. Meaningful values for these parameters had to be adopted; therefore they have been fixed to constant values reported in Table 1. Keeping in mind that the weight of the shear stress is directly affecting the R-value under 45° loading, the variation of the R-value shown in Figs. 7 and 9 can be influenced by the selection of  $a_4$ ,  $b_5$  and  $b_{10}$ , see Eq. 13. The influence on the prediction of earing is somehow more complex, as the earing profile is determined by a combination of anisotropy in yielding and direction of plastic strain rate. Simulations revealed that in particular the height of the ears depends on the choice of the parameter  $a_4$ , but not on  $b_5$  and  $b_{10}$ .

The physical significance of the earing profile has been addressed by many authors by correlating the variation of the R-value with loading direction to the height of the ears after cup-drawing [25, 26]. The quantitative assessment of the earing profile, however, may still include some speculations. A direct correlation is difficult—or maybe impossible to establish, as the formability of magnesium alloys at room temperature is low and cup drawing cannot be conducted experimentally. Recent investigations at elevated temperature (300°C) indicate that for the alloy AZ31 which has a similar texture than ZM21 in the present investigation shows almost no earing after drawing [27]. However, this can be attributed to dynamic recrystallization which generally occurs at temperatures above 200°C.

While comparing Figs. 6 and 8, the differences in fit quality between meeting contours individually and meeting all contours simultaneously is conspicuous. Although many trials of optimization have been conducted it was not possible to get a quantitatively better solution than the one presented in Fig. 8. It can be speculated that this is due to the chosen exponential function or due to the prescribed interval for the parameters. The first has been investigated by using polynomial functions of degree three, which didn't show any significant improvement compared to the exponential functions used here [16]. The latter has been changed during the trials, and it was found that relatively good solutions can be achieved if the parameters  $A_i$ ,  $B_i$  and  $C_i$  are constrained to be positive. This appears to be meaningful in particular for  $C_i$ , as this gives an upper bound for the evolution of  $a_i$ ,  $b_i$  and  $c_i$  with the plastic accumulated strain.

One comment on the underlying hardening assumptions may be justified here. Both, hardening models used in the CP framework and the loadings applied to the RVE in order to generate the contours of plastic work aim on simulating monotonous loading conditions, as the loading history is accounted for by a single (scalar) parameter. In order to capture arbitrary loading history, more sophisticated concepts have to be used—as mentioned in the second chapter. Apparently, in the present paper a simpler approach has been chosen. However, this does not automatically imply that it cannot be used for problems including load path changes or load reversals. For an assessment of the predictive capabilities of this model additional results of mechanical test are necessary, which have not been available to the authors.

**Acknowledgements** The present contribution was finalized during a sabbatical leave of D.S. at the Graduate Institute of Ferrous Technology (G.I.F.T.) of POSTECH, Pohang, Korea as part of an international outgoing fellowship (Marie Curie Actions) of the 7th programme of the European Commission. The authors acknowledge this support and hereby point out that the EU is not responsible for the content of this paper. The authors furthermore like to acknowledge the extensive discussion and the help of M. Nebebe during the realisation of the optimisation code and the help of M. Homayonifar for the discretisation of rolled sheet texture.

## References

1. Kaiser F, et al (2003) Anisotropic properties of magnesium sheet AZ31. In: Kojima Y, et al (eds) Magnesium alloys 2003, Pts 1 and 2. pp 315–320.
2. Kelley EW, Hosford WF (1968) The deformation characteristics of textured magnesium. *Trans Metall Soc AIME* 242:654–661
3. Yoo MH (1981) Slip, twinning, and fracture in hexagonal close-packed metals. *Metall Trans A* 12A:409–418
4. Peirce D, Asaro RJ, Needleman A (1983) Material rate dependence and localized deformation in ductile single crystals. *Acta Metall* 31(12):1051–1076
5. Peirce D, Asaro RJ, Needleman A (1983) Material rate dependence and localized deformation in crystalline solids. *Acta Metall* 31(12):1951–1976
6. Lebensohn RA, Tomé CN (1994) A self-consistent viscoplastic model: prediction of rolling textures of anisotropic polycrystals. *Mater Sci Eng, A* 175(1–2):71–82
7. Staroselsky A, Anand L (2003) A constitutive model for hcp materials deforming by slip and twinning: application to magnesium alloy AZ31B. *Int J Plast* 19(10):1843–1864
8. Lebensohn RA, Tomé CN (1993) A self-consistent anisotropic approach for the simulation of plastic deformation and texture development of polycrystals: application to zirconium alloys. *Acta Metall Mater* 41:2611–2624
9. Graff S, Brocks W, Steglich D (2007) Yielding of magnesium: from single crystal to polycrystalline aggregates. *Int J Plast* 23(12):1957–1978
10. Cazacu O, Barlat F (2004) A criterion for description of anisotropy and yield differential effects in pressure-insensitive metals. *Int J Plast* 20(11):2027–2045
11. Betten J (1979) Über die Konvexität von Fließkörpern isotroper und anisotroper Stoffe. *Acta Mech* 32:233–247
12. Kelley EW, Hosford WF Jr (1968) Plane-strain compression of magnesium and magnesium alloy crystals. *Trans Metall Soc AIME* 242:5–13
13. Lee M-G et al (2008) Constitutive modeling for anisotropic/asymmetric hardening behavior of magnesium alloy sheets. *Int J Plast* 24(4):545–582
14. Ertürk S, et al (2009) Thermo-mechanical modelling of indirect extrusion process for magnesium alloys. In: ESAFORM 2009. Springer
15. Ertürk S (2009) Thermo-mechanical modelling and simulation of magnesium alloys during extrusion process. In Technische Fakultät. Christian-Albrechts Universität: Kiel, pp 101
16. Graff S (2007) Micromechanical modeling of deformation in hcp metals. Technische Universität, Berlin, D
17. Hantzsche K, et al (2007) Magnesium sheet alloys for structural applications. In: Light metals technology
18. Toth LS, Van Houtte P (1992) Discretization techniques for orientation distribution functions. *Textures Microstruct* 19:229–244
19. Asaro RJ (1983) Micromechanics of crystals and polycrystals. *Adv Appl Mech* 23:1–115
20. Asaro RJ (1983) Crystal plasticity. *J Appl Mech Trans ASME* 50:921–934
21. Tadano Y (2010) Polycrystalline behavior analysis of pure magnesium by the homogenization method. *Int J Mech Sci* 52(2):257–265
22. Caceres C, Lukac P (2008) Strain hardening behaviour and the Taylor factor of pure magnesium. *Philos Mag* 88(7):977–989
23. Rechenberg I (1994) Evolutionsstrategie '94. Frommann-Holzboog Verlag, Stuttgart
24. Cazacu O, Plunkett B, Barlat F (2006) Orthotropic yield criterion for hexagonal closed packed metals. *Int J Plast* 22:1171–1194
25. Yoon JW et al (2000) Earing predictions based on asymmetric nonquadratic yield function. *Int J Plast* 16(9):1075–1104
26. Hosford WF, Caddell RM (2007) Metal forming—mechanic and metallurgy, 3rd edn. Cambridge University Press
27. Yi S et al (2009) Mechanical anisotropy and deep drawing behaviour of AZ31 and ZE10 magnesium alloy sheets. *Acta Mater* 58(2):592–605